

1 **Tropopause Evolution in a Rapidly Intensifying Tropical Cyclone: A Static**  
2 **Stability Budget Analysis in an Idealized, Axisymmetric Framework**

3 Patrick Duran\* and John Molinari

4 *University at Albany, State University of New York, Albany, NY*

5 \**Corresponding author address:* Department of Atmospheric and Environmental Sciences, Univer-  
6 sity at Albany, State University of New York, 1400 Washington Avenue, Albany, NY.

7 E-mail: pduran2008@gmail.com

## ABSTRACT

8 Large changes in tropopause-layer static stability are observed during the  
9 rapid intensification (RI) of an idealized, axisymmetric tropical cyclone (TC).  
10 Over the eye, static stability near the tropopause decreases and the cold-point  
11 tropopause height rises by up to 4 km at the storm center. Outside of the eye,  
12 static stability increases considerably just above the cold-point tropopause,  
13 and the tropopause remains near its initial level.

14 A budget analysis reveals that advection contributes to the static stability  
15 tendencies at all times throughout the upper troposphere and lower strato-  
16 sphere. Differential advection is particularly important within the eye, where  
17 it acts to destabilize the layer near and above the cold-point tropopause.  
18 Outside of the eye, a radial-vertical circulation develops during RI, with  
19 strong outflow below the tropopause and weak inflow above. Vertical wind  
20 shear above and below the upper-tropospheric outflow maximum induces tur-  
21 bulence, which provides forcing for both destabilization and stabilization  
22 in the tropopause layer. Meanwhile, as organized convection reaches the  
23 tropopause, radiative heating tendencies at the top of the cirrus canopy gen-  
24 erally act to destabilize the upper troposphere and stabilize the lower strato-  
25 sphere. Turbulent mixing and radiative heating combine to play an important  
26 role in the development of the strong stable layer immediately above the cold-  
27 point tropopause during RI. The results suggest that turbulence and radiation,  
28 alongside advection, play fundamental roles in the upper-level static stability  
29 evolution of TCs.

## 30 **1. Introduction**

31 After undergoing a remarkably rapid intensification (RI), Hurricane Patricia (2015) set a new  
32 record as the strongest tropical cyclone (TC) ever observed in the Western Hemisphere (Kim-  
33 berlain et al. 2016; Rogers et al. 2017). High-altitude dropsonde observations taken during the  
34 Tropical Cyclone Intensity (TCI) experiment captured this RI in unprecedented detail (Doyle et al.  
35 2017). These observations revealed dramatic changes in the structure of the cold-point tropopause  
36 and upper-level static stability as the storm intensified (Duran and Molinari 2018).

37 When Patricia was at tropical storm intensity, shortly before RI commenced, a strong inversion  
38 layer existed just above the cold-point tropopause. During the first half of the RI period, this  
39 inversion layer weakened throughout Patricia’s inner core, with the weakening most pronounced  
40 over the developing eye. By the time the storm reached its maximum intensity of  $95 \text{ m s}^{-1}$ , the  
41 inversion layer over the eye had disappeared almost completely, which was accompanied by a  
42 greater than 1-km increase in the tropopause height. Meanwhile over the eyewall region, the static  
43 stability increased and the tropopause remained near its initial level. The mechanisms that might  
44 have led to this tropopause-layer variability will be investigated in the current paper using idealized  
45 simulations.

46 Despite the importance of tropopause-layer thermodynamics in theoretical models of hurri-  
47 canes (Emanuel and Rotunno 2011; Emanuel 2012), most observational studies of the upper-  
48 tropospheric structure of TCs are decades old. Recently, however, Komaromi and Doyle (2017)  
49 found that stronger TCs tended to have a higher and warmer tropopause over their inner core than  
50 weaker TCs. Their results are consistent with the evolution observed over the inner core of Hur-  
51 ricane Patricia, in which the tropopause height increased and the tropopause temperature warmed  
52 throughout RI (Duran and Molinari 2018).

53 Idealized simulations of a TC analyzed by Ohno and Satoh (2015) suggested that the develop-  
54 ment of an upper-level warm core near the 13-km level acted to decrease the static stability near the  
55 tropopause within the eye (compare their Figs. 9,10). Although the mechanisms that might drive  
56 this static stability evolution have not been examined explicitly, Stern and Zhang (2013) described  
57 the development of the TC warm core using a potential temperature ( $\theta$ ) budget analysis. They  
58 found that radial and vertical advection both played important roles in warm core development  
59 throughout RI, and subgrid-scale diffusion became particularly important during the later stage of  
60 RI. To our knowledge, the only paper that has examined explicitly the static stability evolution in  
61 a modeled TC is Kepert et al. (2016), but their analysis was limited to the boundary layer. The  
62 analysis herein is based upon that of Stern and Zhang (2013), except using a static stability budget  
63 similar to that of Kepert et al. (2016), with a focus on the upper troposphere and lower stratosphere.

## 64 **2. Model Setup**

65 The numerical simulations were performed using version 19.4 of Cloud Model 1 (CM1) de-  
66 scribed in Bryan and Rotunno (2009). The equations of motion were integrated on a 3000-km-  
67 wide, 30-km-deep axisymmetric grid with 1-km horizontal and 250-m vertical grid spacing. The  
68 computations were performed on an  $f$ -plane at 15°N latitude, over a sea surface with constant  
69 temperature of 30.5°C, which matches that observed near Hurricane Patricia (2015; Kimberlain  
70 et al. 2016). Horizontal turbulence was parameterized using the Smagorinsky scheme described  
71 in Bryan and Rotunno (2009, pg. 1773), with a prescribed mixing length that varied linearly from  
72 100 m at a surface pressure of 1015 hPa to 1000 m at a surface pressure of 900 hPa. Vertical  
73 turbulence was parameterized using the formulation of Markowski and Bryan (2016, their Eq. 6),  
74 using an asymptotic vertical mixing length of 100 m. A Rayleigh damping layer was applied out-  
75 side of the 2900-km radius and above the 25-km level to prevent spurious gravity wave reflection

at the model boundaries. Microphysical processes were parameterized using the Thompson et al. (2004) scheme and radiative heating tendencies were computed every two minutes using the Rapid Radiative Transfer Model for GCMs (RRTMG) longwave and shortwave schemes (Iacono et al. 2008). The initial temperature and humidity field was horizontally homogeneous and determined by averaging all Climate Forecast System Reanalysis (CFSR) grid points within 100 km of Patricia's center of circulation at 18 UTC 21 October 2015. The vortex described in Rotunno and Emanuel (1987, their Eq. 37) was used to initialize the wind field, setting all parameters equal to the values used therein.

Although hurricanes simulated in an axisymmetric framework tend to be more intense than those observed in nature, the intensity evolution of this simulation matches reasonably well with that observed in Hurricane Patricia. After an initial spin-up period of about 20 hours, the modeled storm (Fig. 1, blue lines) began an RI period that lasted approximately 30 hours. After this RI, the storm continued to intensify more slowly until the maximum 10-m wind speed reached  $89 \text{ m s}^{-1}$  and the sea-level pressure reached its minimum of 846 hPa, 81 hours into the simulation. Hurricane Patricia (red stars) exhibited a similar intensity evolution prior to its landfall, with an RI period leading to a maximum 10-m wind speed of  $95 \text{ m s}^{-1}$  and a minimum sea-level pressure of 872 hPa.

### 3. Budget Computation

The static stability can be expressed as the squared Brunt-Väisälä frequency:

$$N_m^2 = \frac{g}{T} \left( \frac{\partial T}{\partial z} + \Gamma_m \right) \left( 1 + \frac{T}{R_d/R_v + q_s} \frac{\partial q_s}{\partial T} \right) - \frac{g}{1 + q_t} \frac{\partial q_t}{\partial z}, \quad (1)$$

where  $g$  is gravitational acceleration,  $T$  is temperature,  $R_d$  and  $R_v$  are the gas constants of dry air and water vapor, respectively,  $q_s$  is the saturation mixing ratio,  $q_t$  is the total condensate mixing

ratio, and  $\Gamma_m$  is the moist-adiabatic lapse rate:

$$\Gamma_m = g(1 + q_t) \left( \frac{1 + L_v q_s / R_d T}{c_{pm} + L_v \partial q_s / \partial T} \right), \quad (2)$$

where  $L_v$  is the latent heat of vaporization and  $c_{pm}$  is the specific heat of moist air at constant pressure. In the tropopause layer,  $q_s$ ,  $\partial q_s / \partial T$ , and  $\partial q_t / \partial z$  approach zero. In this limiting case, Eq. 1 reduces to:

$$N^2 = \frac{g}{\theta} \frac{\partial \theta}{\partial z}, \quad (3)$$

where  $\theta$  is the potential temperature.

To compute  $N^2$ , CM1 uses Eq. 1 in saturated environments and Eq. 3 in sub-saturated environments. For simplicity, however, only Eq. 3 will be employed for the budget computations<sup>1</sup>.

Taking the time derivative of Eq. 3 yields the static stability tendency:

$$\frac{\partial N^2}{\partial t} = \frac{g}{\theta} \frac{\partial}{\partial z} \frac{\partial \theta}{\partial t} - \frac{g}{\theta^2} \frac{\partial \theta}{\partial z} \frac{\partial \theta}{\partial t}, \quad (4)$$

where the potential temperature tendency,  $\partial \theta / \partial t$ , can be written, following Bryan (cited 2018):

$$\frac{\partial \theta}{\partial t} = -u \frac{\partial \theta}{\partial r} - w \frac{\partial \theta}{\partial z} + HTURB + VTURB + MP + RAD + DISS \quad (5)$$

Each term on the right-hand side of Eq. 5 represents a  $\theta$  budget variable, each of which is output directly by the model every minute. Since the first term on the right-hand side of Eq. 4 is larger than the second term throughout most of the tropopause layer (not shown), the contribution of each of the terms in Eq. 5 to the  $N^2$  tendency can be interpreted in light of a vertical gradient of each term.

Taking the vertical gradient of the first two terms on the right-hand side of Eq. 5 yields the time tendency of the vertical  $\theta$  gradient due to horizontal and vertical advection<sup>2</sup>:

---

<sup>1</sup>The validity of this approximation will be substantiated later in this section.

<sup>2</sup>These terms include the tendencies due to implicit diffusion in the fifth-order finite differencing scheme, which are separated from the advection

terms in the CM1 budget output

$$\left( \frac{\partial}{\partial t} \frac{\partial \theta}{\partial z} \right)_{adv} = -u \frac{\partial}{\partial r} \frac{\partial \theta}{\partial z} - w \frac{\partial}{\partial z} \frac{\partial \theta}{\partial z} - \frac{\partial u}{\partial z} \frac{\partial \theta}{\partial r} - \frac{\partial w}{\partial z} \frac{\partial \theta}{\partial z}. \quad (6)$$

113 The first two terms on the right-hand side of Eq. 6 represent advection of static stability by the  
 114 radial and vertical wind, respectively. These terms act to rearrange the static stability field, but  
 115 cannot strengthen or weaken static stability maxima or minima. The third and fourth terms on the  
 116 right-hand side of Eq. 6 represent, respectively, the tilting of isentropes in the presence of vertical  
 117 wind shear, and the stretching or squashing of isentropes by vertical gradients of vertical velocity.  
 118 Since these terms involve velocity gradients, they can act to strengthen or weaken static stability  
 119 maxima or minima through differential advection. For example, since the  $\theta$  of the air flowing  
 120 out of the eyewall into the upper-tropospheric outflow layer increases as the TC intensifies,  $\theta$  in-  
 121 creases locally within the outflow layer. This acts to increase  $\partial \theta / \partial z$  below the outflow maximum  
 122 and decrease  $\partial \theta / \partial z$  above, thereby modifying the static stability field. Similarly, the decay of  
 123 updrafts with height at the top of convective towers can act to increase  $\partial \theta / \partial z$  through squashing  
 124 of isentropes.

125 Returning to Eq. 5, HTURB and VTURB are the  $\theta$  tendencies from the horizontal and vertical  
 126 turbulence parameterizations, MP is the tendency from the microphysics scheme, RAD is the  
 127 tendency from the radiation scheme, and DISS is the tendency due to turbulent dissipation. This  
 128 equation neglects Rayleigh damping, since the entire analysis domain lies outside of the regions  
 129 where damping is applied. Each term in Eq. 5 is substituted for  $\partial \theta / \partial t$  in Eq. 4, yielding the  
 130 contribution of each budget term to the static stability tendency. These terms are summed, yielding  
 131 an instantaneous "budget change" in  $N^2$  every minute. The budget changes are then averaged over  
 132 24-hour periods and compared to the total model change in  $N^2$  over that same time period, i.e.:

$$\Delta N_{budget}^2 = \frac{1}{\delta t} \sum_{t=t_0}^{t_0+\delta t} \frac{\partial N^2}{\partial t} \Big|_t \quad (7)$$

$$\Delta N_{model}^2 = N_{t_0+\delta t}^2 - N_{t_0}^2 \quad (8)$$

$$Residual = \Delta N_{model}^2 - \Delta N_{budget}^2 \quad (9)$$

where  $t_0$  is an initial time and  $\delta t$  is 24 hours.

Eqs. 7-9 are plotted for three consecutive 24-hour periods in Fig. 2. For this and all subsequent radial-vertical cross sections, a 1-2-1 smoother is applied once in the radial direction to eliminate  $2\Delta r$  noise that appears in some of the raw model output and calculated fields. The left column of Fig. 2 depicts the model changes computed using Eq. 8, together with Eq. 1 in saturated environments and Eq. 3 in subsaturated environments. The center column depicts the budget changes computed using Eq. 7 together with Eq. 3 throughout the entire domain. Thus, the left column includes the effect of moisture in the  $N^2$  computations, whereas the center column neglects moisture. The right column depicts the residuals, computed using Eq. 9 (i.e. the left column minus the center column.) In every 24-hour period, the budget changes are nearly identical to the model changes, which is reflected in the near-zero residuals in the right column. This indicates that the budget accurately represents the model variability, which implies that the neglect of moisture in the budget computation introduces negligible error within the analysis domain<sup>3</sup>.

In the tropopause layer, some of the budget terms are small enough to be ignored. To determine which of the budget terms are most important, a time series of the contribution of each of the budget terms in Eq. 5 to the tropopause-layer static stability tendency is plotted in Fig. 3. For this figure, each of the budget terms is computed using the method described in Section 3, except with 1-hour averaging intervals instead of 24-hour intervals. The absolute values of these tendencies are then averaged over the radius-height domain of the plots shown in Fig. 2 and plotted as a time

---

<sup>3</sup>This is not the case in the lower- and mid-troposphere, where the residual actually exceeds the budget tendencies in many places, likely due to the neglect of moisture; thus we limit this analysis to the upper troposphere and lower stratosphere.



154 series<sup>4</sup>. Advection (Fig. 3, red line) plays an important role in the mean tropopause-layer static  
155 stability tendency at all times, and vertical turbulence (Fig. 3, blue line) and radiation (Fig. 3, dark  
156 green line) also contribute significantly. The remaining three processes - horizontal turbulence,  
157 microphysics, and dissipative heating - lie atop one another near zero. Although the horizontal  
158 turbulence and microphysics terms can be quite large in the eyewall region, they are negligible  
159 everywhere outside of the eyewall, and do not play important roles in the mesoscale tropopause  
160 variability. Dissipative heating, meanwhile, is relatively small everywhere.

161 The preceding analysis indicates that, at all times, three budget terms dominate the tropopause-  
162 layer static stability tendency: advection, vertical turbulence, and radiation. Variations in the  
163 magnitude and spatial structure of these terms drive the static stability changes depicted in Fig. 2;  
164 subsequent sections will focus on these variations and what causes them.

## 165 4. Results

### 166 a. Static stability evolution

167 The average  $N^2$  over the first day of the simulation (Fig. 4a) indicates the presence of a weak  
168  $N^2$  maximum just above the cold-point tropopause. Over the subsequent 24 hours, during the  
169 RI period, the  $N^2$  within and above this layer decreased within the 25-km radius (Fig. 4b). This  
170 decreasing  $N^2$  corresponded to an increase in the tropopause height within the developing eye,  
171 maximized at the storm center. Outside of the eye, meanwhile, the tropopause height decreased  
172 over the eyewall region (25-60-km radius) and increased only slightly outside of the 60-km ra-  
173 dius. In this outer region, the  $N^2$  maximum just above the tropopause strengthened during RI.

---

<sup>4</sup>It will be seen in subsequent figures that each of the terms contributes both positively and negatively to the  $N^2$  tendency within the analysis domain. Thus, taking an average over the domain tends to wash out the positive and negative contributions. To circumvent this problem, the absolute value of each of the terms is averaged.

174 These trends continued as the storm's intensity leveled off in the 48-72-hour period (Fig. 4c). The  
175 tropopause height increased to nearly 21 km at the storm center and sloped sharply downward to  
176 16.3 km on the inner edge of the eyewall, near the 30 km radius. Static stability outside of the eye,  
177 meanwhile, continued to increase just above the cold-point tropopause. This  $N^2$  evolution closely  
178 follows that observed in Hurricane Patricia (2015; Duran and Molinari 2018). The mechanisms  
179 that led to these  $N^2$  changes will be investigated in the subsequent sections.

## 180 *b. Static stability budget analysis*

181 *(i) 0-24 hours* The weakening of the lower-stratospheric  $N^2$  maximum during the initial spin-up  
182 period is reflected in the total  $N^2$  budget change over this time (Fig. 5a). The layer just above  
183 the cold-point tropopause was characterized by decreasing  $N^2$  (purple shading), maximizing at the  
184 storm center. At and immediately below the tropopause, meanwhile, saw increasing  $N^2$  during this  
185 time period. Although these tendencies extended out to the 200-km radius, they were particularly  
186 pronounced at innermost radii. A comparison of the contributions of advection (Fig. 5b), vertical  
187 turbulence (Fig. 5c), and radiation (Fig. 5d) reveals that advection was the primary driver of the  
188  $N^2$  tendency during this period, acting to stabilize near and just below the tropopause and destabi-  
189 lize above. Although vertical turbulence acted in opposition to advection (i.e. it acted to stabilize  
190 regions that advection acted to destabilize), the magnitude of the advective tendencies was larger,  
191 particularly at the innermost radii. The sum of advection and vertical turbulence (Fig. 5e) almost  
192 exactly replicated the static stability tendencies above the tropopause. Radiative tendencies, mean-  
193 while, (Fig. 5d) acted to destabilize the layer below about 16 km and stabilize the layer between  
194 16 and 17 km. The sum of advection, vertical turbulence, and radiation (Fig. 5f) reproduces the  
195 total change in  $N^2$  almost exactly.

196 (ii) *24-48 hours* During the RI period,  $N^2$  within the eye generally decreased above 16 km and  
197 increased below (Fig. 6a), with the destabilization above 16 km maximizing near the level of the  
198 mean cold-point tropopause. These tendencies at the innermost radii were driven almost entirely  
199 by advection (Fig. 6b); vertical turbulence (Fig. 6c) and radiation (Fig. 6d) contributed negligibly  
200 to the static stability tendencies in this region.

201 Outside of the eye, the  $N^2$  evolution exhibited alternating layers of positive and negative tenden-  
202 cies. Near and above 18 km existed an upward-sloping region of decreasing  $N^2$  that extended out  
203 to the 180-km radius. In this region, neither vertical turbulence nor radiation exhibited negative  $N^2$   
204 tendencies; advection was the only forcing for this destabilization. Immediately below this layer,  
205 just above the cold-point tropopause, was a region of increasing  $N^2$  that sloped upward from 17 km  
206 near the 30-km radius to just below 18 km outside of the 100-km radius. Advection and vertical  
207 turbulence both contributed to this positive  $N^2$  tendency, with advection playing an important role  
208 below about 17.5 km and and turbulence playing an important role above. The sum of advection  
209 and turbulence (Fig. 6e) reveals two discontinuous regions of increasing  $N^2$  in the 17-18-km layer  
210 rather than one contiguous region. The addition of radiation to these two terms, however, (Fig. 6f)  
211 provides the link between these two regions, indicating that radiation also plays a role in strength-  
212 ening the stable layer just above the tropopause. In the 16-17-km layer, just below the cold-point  
213 tropopause, a horizontally-extensive layer of destabilization also was forced by a combination of  
214 advection, vertical turbulence, and radiation. The sum of advection and vertical turbulence ac-  
215 counts for only a portion of the decreasing  $N^2$  in this layer, and actually indicates forcing for  
216 stabilization near the 50-km radius and outside of the 130-km radius. Radiative tendencies over-  
217 come this forcing for stabilization in both of these regions to produce the radially-extensive region  
218 of destabilization observed just below the tropopause.

219 The sum of advection, vertical turbulence, and radiation (Fig. 6f) once again closely follows  
220 the observed  $N^2$  variability, except in the eyewall region, where the neglect of latent heating and  
221 horizontal turbulence introduces some differences.

222 (iii) 48-72 hours After the storm's maximum wind speed leveled off near  $80 \text{ m s}^{-1}$ , the magnitude  
223 of the static stability tendencies within the eye decreased to near zero (Fig. 7a).

224 Outside of the eye, however,  $N^2$  continued to decrease in the layer immediately surrounding the  
225 tropopause. The sum of advection and vertical turbulence (Fig. 7e) indicates that the increase of  
226  $N^2$  observed in the 17-18-km layer and inside of the 80-km radius cannot be attributed to these  
227 processes, since the sum of these two terms provided forcing for destabilization. Instead, radiation  
228 (Fig. 7d) provided the forcing for stabilization in this region. Outside of the 80-km radius, both  
229 advection (Fig. 7b) and vertical turbulence (Fig. 7c) provided forcing for stabilization near and  
230 just above the 18-km level. The sum of the two terms (Fig. 7e) indicates increasing  $N^2$  near the  
231 18-km level everywhere outside of the 80-km radius, but this stabilization is slightly weaker in  
232 the 90-120-km radial band than the observed value. The addition of radiation (Fig. 7f) provided  
233 the extra forcing for stabilization required to account for the observed increase in  $N^2$ . Outside  
234 of the 120-km radius, the region of radiative forcing for stabilization sloped downward, and the  
235 increase in  $N^2$  observed near 18 km can be explained entirely by a combination of advection and  
236 vertical turbulence. The layer of decreasing  $N^2$  observed near the tropopause was forced primarily  
237 by vertical turbulence and radiation. Within most of this region, advection provided strong forcing  
238 for stabilization, but this forcing was outweighed by the negative  $N^2$  tendencies induced by a  
239 combination of vertical turbulence and radiation.

## 5. Discussion

### *a. The role of advection*

Advection played an important role in the tropopause-layer  $N^2$  evolution at all stages of intensification, but for brevity, this section will focus only on the RI (24-48-hour) period. To investigate the advective processes more closely, the individual contributions of horizontal and vertical advection during the RI period are shown in Fig. 8, along with the corresponding time-mean radial and vertical velocities and  $\theta$ . The  $N^2$  tendencies due to the two advective components (Fig. 8a,b) exhibited strong cancellation, consistent with flow that was nearly isentropic. There were, however, many regions in which flow crossed  $\theta$  surfaces; this flow accounted for all non-zero  $N^2$  tendencies due to advection previously seen in Fig. 6b.

During the RI period, strong radial and vertical circulations developed near the tropopause (Fig. 8c,d), which forced high-magnitude  $N^2$  tendencies due to advection (Fig. 8a,b). A layer of strong outflow formed at and below the tropopause during this period, with the outflow maximum (dashed cyan line) curving from the 14-km level at the 50-km radius to just below the 16-km level outside of the 80-km radius (Fig. 8c). Notably, the  $N^2$  tendency due to horizontal advection (Fig. 8a) tended to switch signs at this line, with stabilization below the outflow maximum and destabilization above. This is consistent with the outflow layer carrying air with increasingly large  $\theta$  from the eyewall to large radii as the storm intensified. This increase in  $\theta$  maximized near the outflow maximum, which acted to decrease  $\partial\theta/\partial z$  above the outflow maximum and increase it below. This mechanism is the same as that discussed in Trier and Sharman (2009), in which vertical wind shear in the outflow layer of a mesoscale convective system acted to modify the upper-tropospheric static stability through differential advection of isentropes.

262 Meanwhile in the lower stratosphere, a thin layer of  $2\text{--}4\text{ m s}^{-1}$  inflow developed a few hundred  
263 meters above the tropopause, similar to that which was observed in Hurricane Patricia (2015;  
264 Duran and Molinari 2018) and in previous modeling studies (e.g. Ohno and Satoh 2015; Kieu et al.  
265 2016). Since the isentropes in this layer sloped slightly upward with radius (i.e.  $\partial\theta/\partial r < 0$ ), this  
266 inflow acted to import lower  $\theta$  air from outer radii to inner radii. Since the negative  $\theta$  tendencies  
267 maximized at the level of maximum inflow, the layer below the inflow maximum destabilized and  
268 the layer above stabilized (Fig. 8a).

269 Curiously, horizontal advection contributed to the  $N^2$  tendency everywhere within the eye,  
270 even though the mean radial velocity there was near zero. Close examination of the model out-  
271 put revealed that these tendencies were forced by advective processes associated with inward-  
272 propagating waves. Although the radial velocity perturbations induced by these waves averaged  
273 out to zero, the advective tendencies forced by the radial velocity perturbations did not. Addition-  
274 ally, when these waves reached  $r=0$ , a dipole of vertical velocity resulted, with ascent above and  
275 descent below. For reasons that remain unclear, the regions of ascent were more persistent than the  
276 regions of descent, which resulted in the mean ascent observed near  $r=0$  above 17 km in Fig. 8b.

277 Vertical advection also played an important role in the tropopause-layer static stability evolution.  
278 Within the eye, subsidence dominated below 17 km, while mean ascent existed near the storm  
279 center above 17 km. Although the magnitude of the subsidence was larger at lower altitudes,  
280  $\partial\theta/\partial z$  was smaller there. Because  $\partial\theta/\partial z$  was smaller, the subsidence at lower levels could not  
281 accomplish as much warming as the subsidence at higher levels in the eye, consistent with the  
282 results of Stern and Zhang (2013). As a result, vertical advection within the eye acted to stabilize  
283 the layer below 16 km during RI.

284 Outside of the 27-km radius, ascent dominated the troposphere, while a 1.5-km-deep layer of  
285 descent existed immediately above the tropopause. These regions of ascent and descent converged

just above the tropopause; this convergence acted to compact the isentropes in this layer and increase the static stability. Above the lower-stratospheric subsidence maximum, meanwhile, vertical advection acted to decrease  $N^2$ . Below the tropopause, differential vertical advection increased  $N^2$  within the eyewall region and also at larger radii above the vertical velocity maximum at larger radii. Outside of the eyewall and below the vertical velocity maximum, meanwhile, differential vertical advection acted to decrease  $N^2$ .

Comparing the  $N^2$  tendencies forced by horizontal (Fig. 8a) and vertical (Fig. 8b) advection to the total advective tendency seen in Fig. 6b reveals that horizontal advective tendencies dominated the troposphere, while vertical advective tendencies dominated the layer near and above the tropopause. Thus, tilting of isentropes in the vicinity of the upper-tropospheric outflow maximum appears to be the most important process governing the  $N^2$  tendency in the troposphere, whereas convergence of vertical velocity appears to be the most important process near the tropopause.

#### *b. The role of radiation*

During the initial spin-up period (0-24 hours; Fig. 9a), convection was not deep enough to deposit large quantities of ice near the tropopause and create a persistent cirrus canopy. Due to the lack of ice particles, the radiative heating tendencies during this period (Fig. 9b) were relatively small and confined to the region above a few particularly strong, although transient, convective towers. During RI (24-48 hours), the eyewall updraft strengthened and a radially-extensive cirrus canopy developed near the tropopause (Fig. 9c). The enhanced vertical gradient of ice mixing ratio at the top of the cirrus canopy induced strong diurnal-mean radiative cooling near the tropopause (Fig. 9d). This cooling exceeded  $0.6 \text{ K h}^{-1}$  in some places and sloped downward from the lower stratosphere into the upper troposphere, following the top of the cirrus canopy. A small radiative warming maximum also appeared outside of the 140-km radius below this region of cooling. These

309 results broadly agree with those of Bu et al. (2014; see their Fig. 11a), whose CM1 simulations  
310 produced a  $0.3 \text{ K h}^{-1}$  diurnally-averaged radiative cooling at the top of the cirrus canopy and  
311 radiative warming within the cloud that maximized near the 200-km radius. This broad region  
312 of radiative cooling acted to destabilize the layer below the cooling maximum and stabilize the  
313 layer above, which can be seen in Fig. 6d. The small area of net radiative heating outside of the  
314 140-km radius enhanced the destabilization above 16 km in this region and produced a thin layer  
315 of stabilization in the 15-16-km layer.

316 After the TC's RI period completed (48-72 hours), strong radiative cooling remained near the  
317 tropopause at inner radii (Fig. 9f), sloping downward with the top of the cirrus canopy to below  
318 the tropopause at outer radii. Cooling rates exceeded  $1 \text{ K h}^{-1}$  just above the tropopause between  
319 the 30- and 70-km radii. This value is more than three times the maximum cooling rate of  $0.3 \text{ K h}^{-1}$   
320 observed by Bu et al. (2014), a discrepancy that is a consequence of their larger vertical grid  
321 spacing compared to that used here, along with a contribution from differing radiation schemes. To  
322 compare our results to those of Bu et al. (2014), we ran a simulation identical to that described in  
323 Section 2, except using the NASA-Goddard radiation scheme and 625-m vertical grid spacing, to  
324 match those of Bu et al. (2014). This simulation produced a maximum 24-hour-average radiative  
325 cooling rate of  $0.3 \text{ K h}^{-1}$ , which agrees with that shown in Bu et al. (2014). Another simulation  
326 using 625-m vertical grid spacing and RRTMG radiation produced 24-hour-average cooling rates  
327 of up to  $0.6 \text{ K h}^{-1}$ , which is consistent with the WRF simulations of Bu et al. (2014). This suggests  
328 that vertical grid spacing smaller than 625 m is necessary to resolve properly the radiative cooling  
329 at the top of the cirrus canopy, and that the results can be quite sensitive to the radiation scheme  
330 used.

331 Meanwhile below the tropopause, time-mean radiative warming spread from 30- to 160-km  
332 radius within the cirrus canopy. The existence of radiative cooling overlying radiative warming in



333 this region led to radiatively-forced destabilization at and below the tropopause, as was observed  
334 in Fig. 7d. Beneath the warming layer existed a region of forcing for stabilization, while a much  
335 stronger region of forcing for stabilization existed in the lower stratosphere, above the cooling  
336 maximum.

337 The results herein suggest that radiative heating tendencies played an important role in destabi-  
338 lizing the upper troposphere and stabilizing the lower stratosphere after the cirrus canopy devel-  
339 oped.

### 340 *c. The role of turbulent mixing*

341 Although vertical turbulence always acts to eliminate vertical gradients of  $\theta$ , this adjustment  
342 toward a neutral state only occurs where the mixing takes place. If turbulence occurs in a stably-  
343 stratified layer, it will act to decrease  $\theta$  at the top of the layer and increase it below. Just above and  
344 just below the mixed layer, however, the  $\theta$  profile remains undisturbed. Consequently, although  
345 turbulent mixing acts to decrease  $\partial\theta/\partial z$  in the layer in which it is occurring, it actually increases  
346  $\partial\theta/\partial z$  just below and just above the layer. These vertical gradients of turbulent mixing are quite  
347 important, particularly on the flanks of the upper-tropospheric outflow jet.

348 Two distinct maxima of vertical eddy diffusivity developed in the tropopause layer as the storm  
349 intensified (Fig. 10). Comparison of these turbulent regions to the  $N^2$  tendencies in Figs. 6c and  
350 7c reveals that the layers in which vertical eddy diffusivity maximized corresponded to layers of  
351 destabilization due to vertical turbulence. Just outside of these layers, however, vertical turbulence  
352 acted to increase  $N^2$ . The large vertical gradient of vertical eddy diffusivity near the tropopause  
353 played an important role in developing the lower-stratospheric stable layer during RI. This supports  
354 the hypothesized role of turbulence in setting the outflow-layer  $\theta$  stratification in Rotunno and  
355 Emanuel (1987).

## 6. Conclusions

The simulated  $N^2$  evolution shown herein closely matched that observed during the RI of Hurricane Patricia (2015). Three processes dominated the  $N^2$  variability in the upper troposphere and lower stratosphere: advection, radiation, and vertical turbulence. Radiation and vertical turbulence played particularly important roles in developing the strong  $N^2$  maximum just above the cold-point tropopause during RI. Since these two processes are parameterized, and radiation closely depends on yet another parameterized process (microphysics), the tropopause-layer  $N^2$  variability could be quite sensitive to the assumptions inherent to the parameterizations used. A better understanding of the microphysical characteristics of the TC cirrus canopy, its interaction with radiation, and outflow-layer turbulence is critical to understanding the tropopause-layer  $N^2$  evolution.

In this paper, all of the variables were averaged over a full diurnal cycle to eliminate the effects of diurnal variability and isolate the overall storm evolution. Diurnal variations in static stability near the tropopause are potentially of interest with respect to the tropical cyclone diurnal cycle, however, and will be the subject of future work.

*Acknowledgments.* We are indebted to George Bryan for his continued development and support of Cloud Model 1. We also thank Jeffrey Kepert, Robert Fovell, and Erika Navarro for helpful conversations related to this work. This research was supported by NSF Grant #1636799.

## APPENDIX

### Sensitivity experiments

The simulations exhibited some sensitivity to the initial thermodynamic profile and the prescribed vertical mixing length. Although the details of the intensification and the tropopause-layer

377  $N^2$  evolution varied when these quantities were changed, the conclusions of the paper remain  
378 unchanged.

379 *a. Sensitivity to the initial thermodynamic profile*

380 A number of sensitivity experiments were conducted using a variety of initial soundings. Chang-  
381 ing the initial temperature and humidity profiles affected the timing of the onset of organized deep  
382 convection and the rapidity of intensification. In all simulations, however, convection eventually  
383 penetrated to the tropopause, at which time vertical turbulence and radiation combined with ad-  
384 vection to adjust the  $N^2$  profile toward that which was observed in the control run. By the end of  
385 the RI period in every simulation, all three processes were actively modifying the  $N^2$  profile near  
386 the tropopause.

387 As an example, 24-hour averages of  $N^2$  are plotted in Fig. A1 for a simulation that was identical  
388 to that used in this paper, except the initial sounding was determined by averaging every CFSR  
389 grid point within 1000 km of TC Patricia’s storm center at 18 UTC 21 October 2015 instead of  
390 averaging only within the 100-km radius. Although the lower-stratospheric stable layer developed  
391 more slowly and was weaker than that shown in Fig. 4, the overall evolution was quite similar and  
392 the same budget terms dominated the  $N^2$  evolution.

393 *b. Sensitivity to the vertical mixing length*

394 The rate of turbulent mixing in the Smagorinsky scheme used herein is highly dependent on a  
395 prescribed length scale. The vertical mixing length used in this paper (100 m) was based on the  
396 sensitivity experiments of Bryan (2012). Prescribing a smaller mixing length produces smaller  
397  $\theta$  tendencies due to turbulence, but even with a mixing length on the low end of those tested  
398 by Bryan (2012), turbulence still played an important role in the tropopause-layer  $N^2$  evolution.

399 Fig. A2 shows the 24-hour-averaged contributions of turbulent mixing to the  $N^2$  evolution from  
400 a simulation identical to that used in this paper, except with a vertical mixing length of 50 m. At  
401 all times, vertical turbulence still played an important role in the tropopause-layer  $N^2$  evolution,  
402 particularly during the latter stages of RI (48-72 hours).

## 403 References

- 404 Bryan, G. H., 2012: Effects of surface exchange coefficients and turbulence length scales on the  
405 intensity and structure of numerically simulated hurricanes. *Mon. Wea. Rev.*, **140**, 1125–1143.
- 406 Bryan, G. H., cited 2018: The governing equations for CM1. [Available online at [http://www2.mmm.ucar.edu/people/bryan/cm1/cm1\\_equations.pdf](http://www2.mmm.ucar.edu/people/bryan/cm1/cm1_equations.pdf)].
- 407
- 408 Bryan, G. H., and R. Rotunno, 2009: The maximum intensity of tropical cyclones in axisymmetric  
409 numerical model simulations. *Mon. Wea. Rev.*, **137**, 1770–1789.
- 410 Bu, Y. P., R. G. Fovell, and K. L. Corbosiero, 2014: Influence of cloud-radiative forcing on tropical  
411 cyclone structure. *J. Atmos. Sci.*, **71**, 1644–1622.
- 412 Doyle, J. D., and Coauthors, 2017: A view of tropical cyclones from above: The Tropical Cyclone  
413 Intensity (TCI) Experiment. *Bull. Amer. Meteor. Soc.*, **98**, 2113–2134.
- 414 Duran, P., and J. Molinari, 2018: Dramatic inner-core tropopause variability during the rapid  
415 intensification of Hurricane Patricia (2015). *Mon. Wea. Rev.*, **146**, 119–134.
- 416 Emanuel, K., 2012: Self-stratification of tropical cyclone outflow. Part II: Implications for storm  
417 intensification. *J. Atmos. Sci.*, **69**, 988–996.
- 418 Emanuel, K., and R. Rotunno, 2011: Self-stratification of tropical cyclone outflow. Part I: Impli-  
419 cations for storm structure. *J. Atmos. Sci.*, **68**, 2236–2249.

Iacono, M. J., J. S. Delamere, E. J. Mlawer, M. W. Shephard, S. A. Clough, and W. D. Collins,  
 2008: Radiative forcing by long-lived greenhouse gases: Calculations with the AER radiative  
 transfer models. *J. Geophys. Res.*, **113** (D13103).

Kepert, J. D., J. Schwendike, and H. Ramsay, 2016: Why is the tropical cyclone boundary layer  
 not "well mixed"? *J. Atmos. Sci.*, **73**, 957–973.

Kieu, C., V. Tallapragada, D.-L. Zhang, and Z. Moon, 2016: On the development of double warm-  
 core structures in intense tropical cyclones. *J. Atmos. Sci.*, **73**, 4487–4506.

Kimberlain, T. B., E. S. Blake, and J. P. Cangialosi, 2016: Tropical cyclone report: Hurricane  
 Patricia. National Hurricane Center. [Available online at [www.nhc.noaa.gov](http://www.nhc.noaa.gov)].

Komaromi, W. A., and J. D. Doyle, 2017: Tropical cyclone outflow and warm core structure as  
 revealed by HS3 dropsonde data. *Mon. Wea. Rev.*, **145**, 1339–1359.

Markowski, P. M., and G. H. Bryan, 2016: LES of laminar flow in the PBL: A potential problem  
 for convective storm simulations. *Mon. Wea. Rev.*, **144**, 1841–1850.

Ohno, T., and M. Satoh, 2015: On the warm core of a tropical cyclone formed near the tropopause.  
*J. Atmos. Sci.*, **72**, 551–571.

Rogers, R. F., S. Aberson, M. M. Bell, D. J. Cecil, J. D. Doyle, J. Morgerman, L. K. Shay, and  
 C. Velden, 2017: Re-writing the tropical record books: The extraordinary intensification of  
 Hurricane Patricia (2015). *Bull. Amer. Meteor. Soc.*, **98**, 2091–2112.

Rotunno, R., and K. A. Emanuel, 1987: An air-sea interaction theory for tropical cyclones. Part II:  
 Evolutionary study using a nonhydrostatic axisymmetric numerical model. *J. Atmos. Sci.*, **44**,  
 542–561.

- 441 Stern, D. P., and F. Zhang, 2013: How does the eye warm? Part I: A potential temperature budget  
442 analysis of an idealized tropical cyclone. *J. Atmos. Sci.*, **70**, 73–89.
- 443 Thompson, G., R. M. Rasmussen, and K. Manning, 2004: Explicit forecasts of winter precipitation  
444 using an improved bulk microphysics scheme. Part I: Description and sensitivity analysis. *Mon.*  
445 *Wea. Rev.*, **132**, 519–542.
- 446 Trier, S. B., and R. D. Sharman, 2009: Convection-permitting simulations of the environment sup-  
447 porting widespread turbulence within the upper-level outflow of a mesoscale convective system.  
448 *Mon. Wea. Rev.*, **137**, 1972–1990.

## 449 LIST OF FIGURES

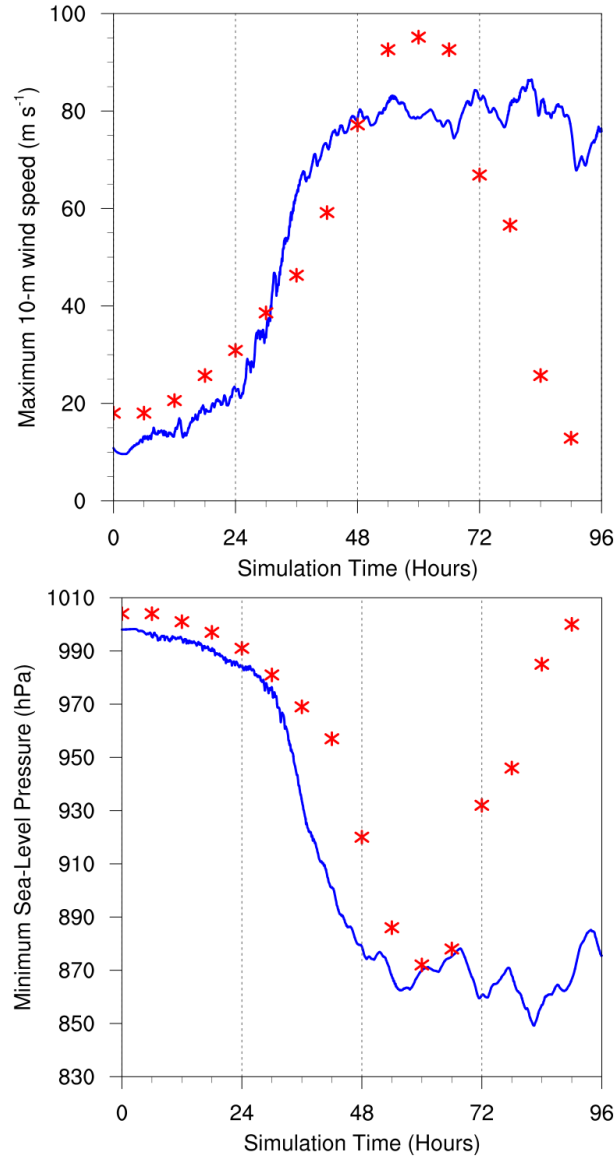
- 450 **Fig. 1.** The maximum 10-m wind speed (top panel;  $\text{m s}^{-1}$ ) and minimum sea-level pressure (bottom  
451 panel; hPa) in the simulated storm (blue lines; plotted every minute) and from Hurricane  
452 Patricia's best track (red stars; plotted every six hours beginning at the time Patricia attained  
453 tropical storm intensity). The rapid weakening during the later stage of Patricia's lifetime  
454 was induced by landfall. . . . . 26
- 455 **Fig. 2.** Left panels: Twenty-four-hour changes in squared Brunt-Väisälä frequency ( $N^2$ ;  $10^{-4} \text{ s}^{-2}$ )  
456 computed using Eq. 8 over (top row) 0-24 hours, (middle row) 24-48 hours, (bottom row)  
457 48-72 hours. Middle Panels: The  $N^2$  change over the same time periods computed using Eqs.  
458 4-7, Right Panels: The budget residual over the same time periods, computed by subtracting  
459 the budget change (middle column) from the model change (left column). Orange lines  
460 represent the cold-point tropopause height averaged over the same time periods. . . . . 27
- 461 **Fig. 3.** Time series of the contribution of each of the budget terms to the time tendency of the  
462 squared Brunt-Väisälä frequency ( $N^2$ ;  $10^{-4} \text{ s}^{-2}$ ). For each budget term, the absolute value  
463 of the  $N^2$  tendency is averaged temporally over 1-hour periods (using output every minute),  
464 and spatially in a region extending from 0 to 200 km radius and 14 to 21 km altitude. . . . . 28
- 465 **Fig. 4.** Twenty-four-hour averages of squared Brunt-Väisälä frequency ( $N^2$ ;  $10^{-4} \text{ s}^{-2}$ ) over (a) 0-24  
466 hours, (b) 24-48 hours, (c) 48-72 hours. Orange lines represent the cold-point tropopause  
467 height averaged over the same time periods. . . . . 29
- 468 **Fig. 5.** (a) Total change in  $N^2$  over the 0-24-hour period ( $10^{-4} \text{ s}^{-2} (24 \text{ h})^{-1}$ ) and the contributions to  
469 that change from (b) the sum of horizontal and vertical advection, (c) vertical turbulence, (d)  
470 longwave and shortwave radiation, (e) the sum of horizontal advection, vertical advection,

471	and vertical turbulence, and (f) the sum of horizontal advection, vertical advection, vertical	
472	turbulence, and longwave and shortwave radiation. Orange lines represent the cold-point	
473	tropopause height averaged over the 0-24-hour period. . . . .	31
474	<b>Fig. 6.</b> As in Fig. 5, but for the 24-48-hour period. . . . .	32
475	<b>Fig. 7.</b> As in Fig. 5, but for the 48-72-hour period. . . . .	33
476	<b>Fig. 8.</b> The contributions to the change in $N^2$ over the 24-48-hour period ( $10^{-4} \text{ s}^{-2} (24 \text{ h})^{-1}$ ) by	
477	(a) horizontal advection and (b) vertical advection. (c) The radial velocity ( $\text{m s}^{-1}$ ; filled con-	
478	tours), potential temperature (K; thick black contours), cold-point tropopause height (orange	
479	line), and level of maximum outflow (dashed cyan line) averaged over the 24-48-hour period.	
480	(d) The vertical velocity ( $\text{cm s}^{-1}$ ; filled contours), potential temperature (K; thick black con-	
481	tours), and cold-point tropopause height (orange line) averaged over the 24-48-hour period.	
482	34	
483	<b>Fig. 9.</b> Ice mixing ratio ( $\text{g kg}^{-1}$ ) and cold-point tropopause height (orange lines) averaged over (a)	
484	0-24 hours, (c) 24-48 hours, and (e) 48-72 hours. Radiative heating rate ( $\text{K h}^{-1}$ ) and cold-	
485	point tropopause height (orange lines) averaged over (b) 0-24 hours, (d) 24-48 hours, and (f)	
486	48-72 hours. . . . .	36
487	<b>Fig. 10.</b> Vertical eddy diffusivity ( $\text{m}^2 \text{ s}^{-2}$ ; filled contours), cold-point tropopause height (cyan lines),	
488	and radial velocity ( $\text{m s}^{-1}$ ; thick black lines) averaged over (a) 0-24 hours, (b) 24-48 hours,	
489	and (c) 48-72 hours. . . . .	37
490	<b>Fig. A1.</b> Twenty-four-hour averages of squared Brunt-Väisälä frequency ( $N^2$ ; $10^{-4} \text{ s}^{-2}$ ) over (a) 0-24	
491	hours, (b) 24-48 hours, (c) 48-72 hours, and (d) 72-96 hours for the simulation described	



492 in Appendix Aa. Orange lines represent the cold-point tropopause height averaged over the  
 493 same time periods. . . . . 38

494 **Fig. A2.** The contribution of vertical turbulence to the  $N^2$  variability ( $10^{-4} \text{ s}^{-2} (24 \text{ h})^{-1}$ ) averaged  
 495 over (a) 0-24 hours, (b) 24-48 hours, (c) 48-72 hours, and (d) 72-96 hours for the simulation  
 496 described in Appendix Ab. Orange lines represent the cold-point tropopause height averaged  
 497 over the same time periods. . . . . 39



498 FIG. 1. The maximum 10-m wind speed (top panel;  $\text{m s}^{-1}$ ) and minimum sea-level pressure (bottom panel;  
 499 hPa) in the simulated storm (blue lines; plotted every minute) and from Hurricane Patricia's best track (red stars;  
 500 plotted every six hours beginning at the time Patricia attained tropical storm intensity). The rapid weakening  
 501 during the later stage of Patricia's lifetime was induced by landfall.

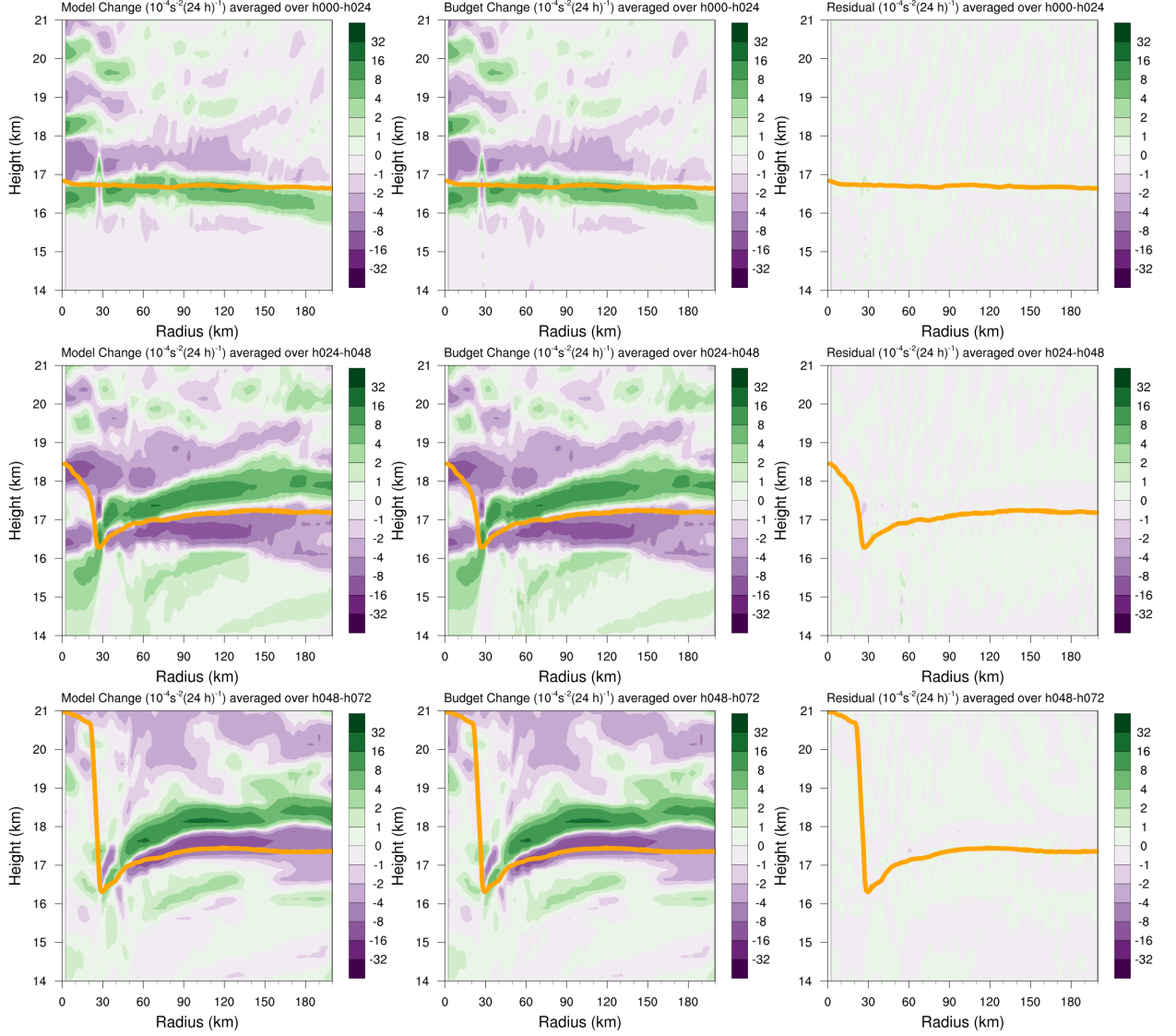


FIG. 2. Left panels: Twenty-four-hour changes in squared Brunt-Väisälä frequency ( $N^2$ ;  $10^{-4} \text{ s}^{-2}$ ) computed using Eq. 8 over (top row) 0-24 hours, (middle row) 24-48 hours, (bottom row) 48-72 hours. Middle Panels: The  $N^2$  change over the same time periods computed using Eqs. 4-7, Right Panels: The budget residual over the same time periods, computed by subtracting the budget change (middle column) from the model change (left column). Orange lines represent the cold-point tropopause height averaged over the same time periods.

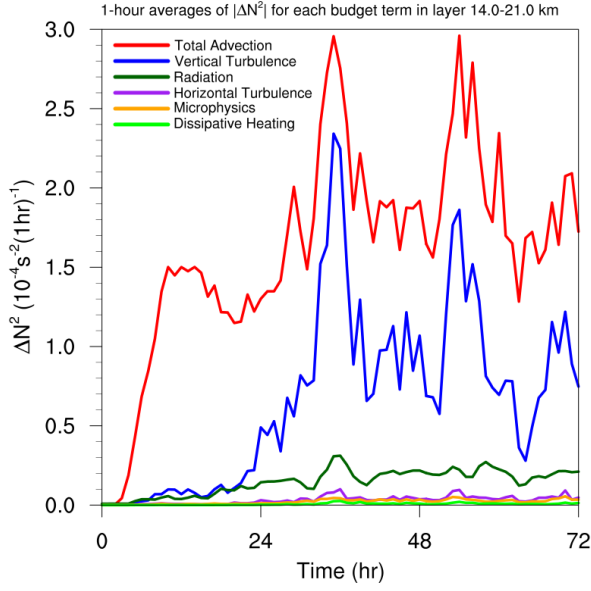


FIG. 3. Time series of the contribution of each of the budget terms to the time tendency of the squared Brunt-Väisälä frequency ( $N^2$ ;  $10^{-4} \text{ s}^{-2}$ ). For each budget term, the absolute value of the  $N^2$  tendency is averaged temporally over 1-hour periods (using output every minute), and spatially in a region extending from 0 to 200 km radius and 14 to 21 km altitude.

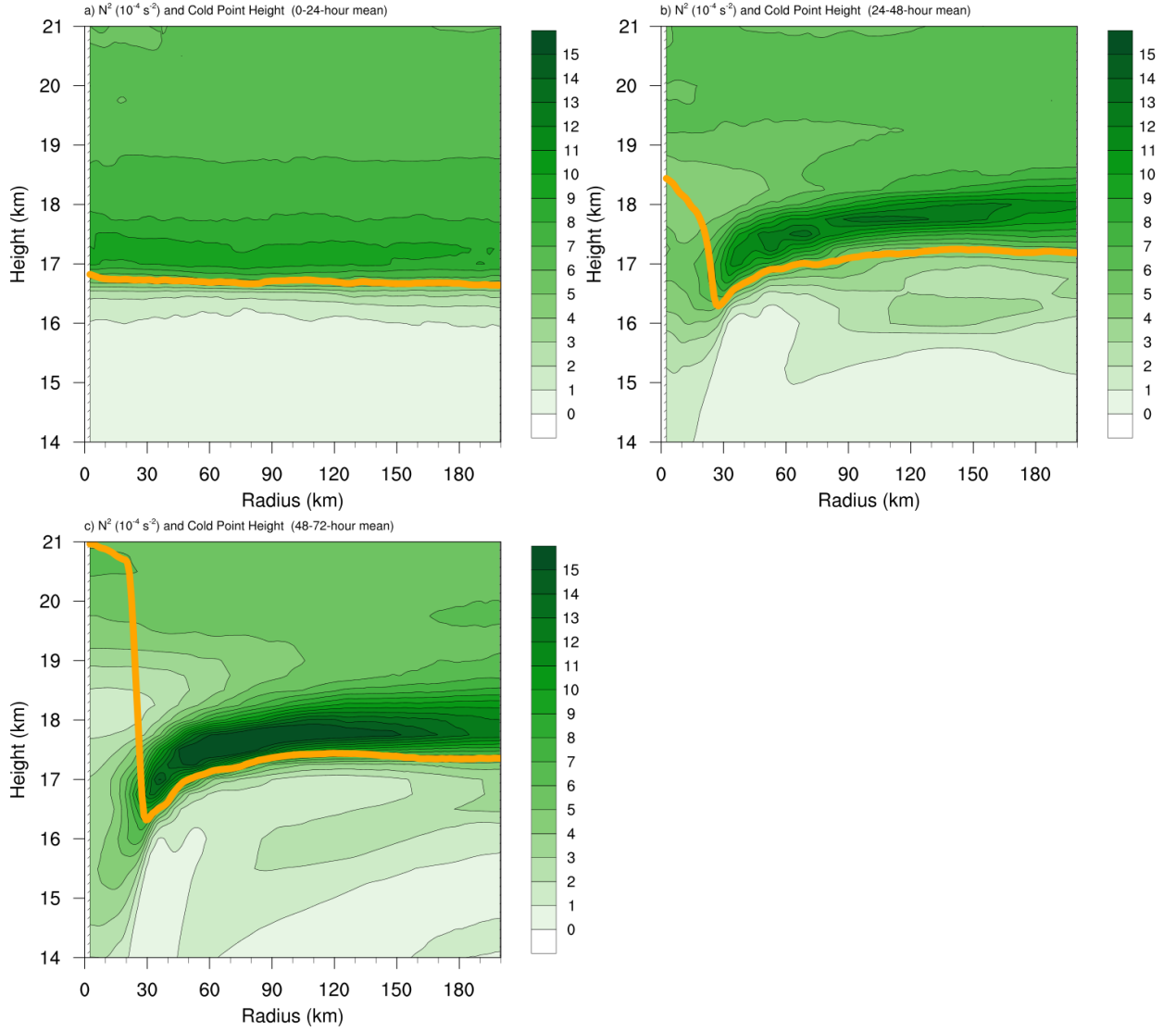
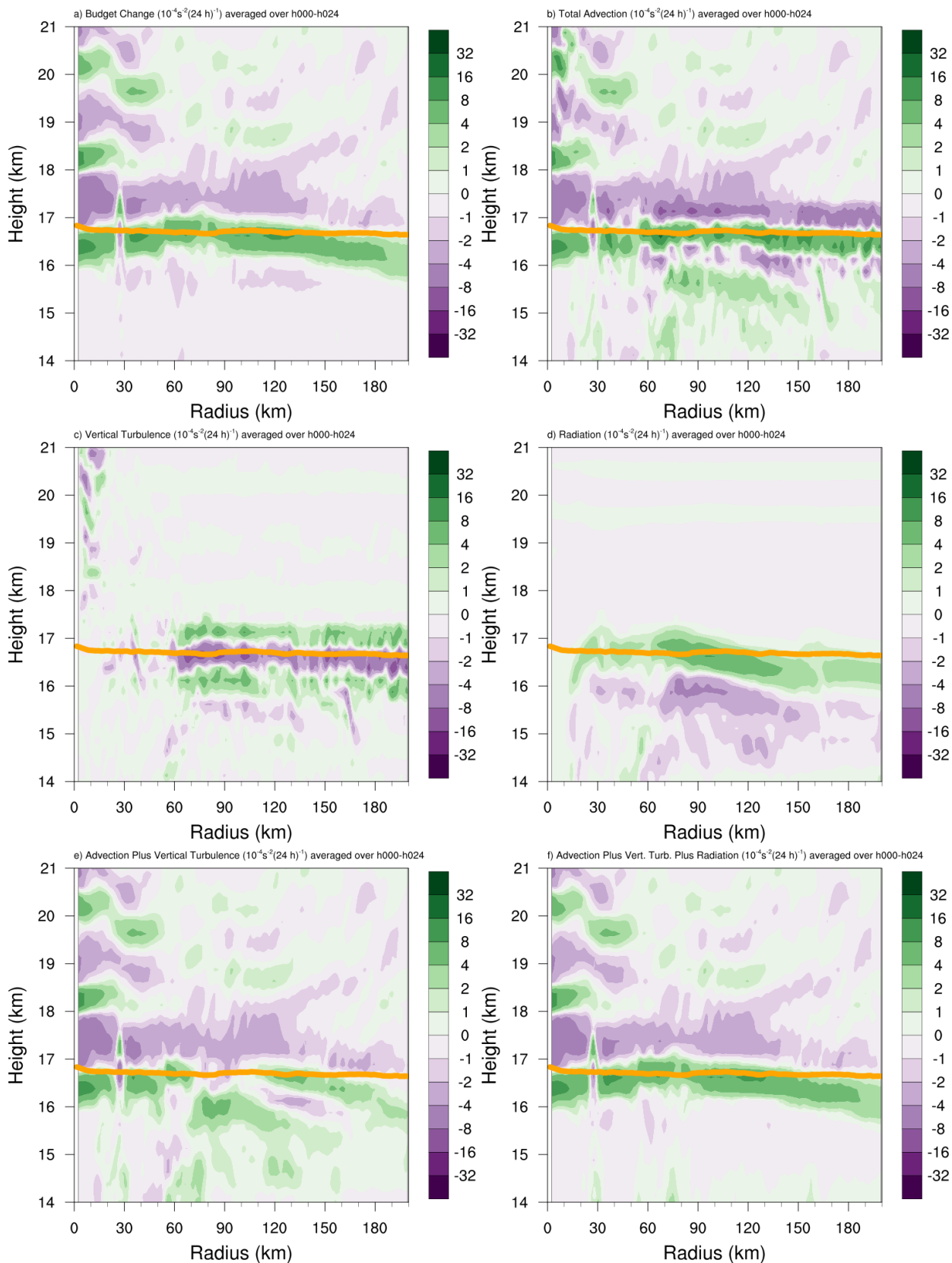


FIG. 4. Twenty-four-hour averages of squared Brunt-Väisälä frequency ( $N^2$ ;  $10^{-4} \text{ s}^{-2}$ ) over (a) 0-24 hours, (b) 24-48 hours, (c) 48-72 hours. Orange lines represent the cold-point tropopause height averaged over the same time periods.



514 FIG. 5. (a) Total change in  $N^2$  over the 0-24-hour period ( $10^{-4} \text{ s}^{-2} (24 \text{ h})^{-1}$ ) and the contributions to that change  
515 from (b) the sum of horizontal and vertical advection, (c) vertical turbulence, (d) longwave and shortwave  
516 radiation, (e) the sum of horizontal advection, vertical advection, and vertical turbulence, and (f) the sum of  
517 horizontal advection, vertical advection, vertical turbulence, and longwave and shortwave radiation. Orange  
518 lines represent the cold-point tropopause height averaged over the 0-24-hour period.

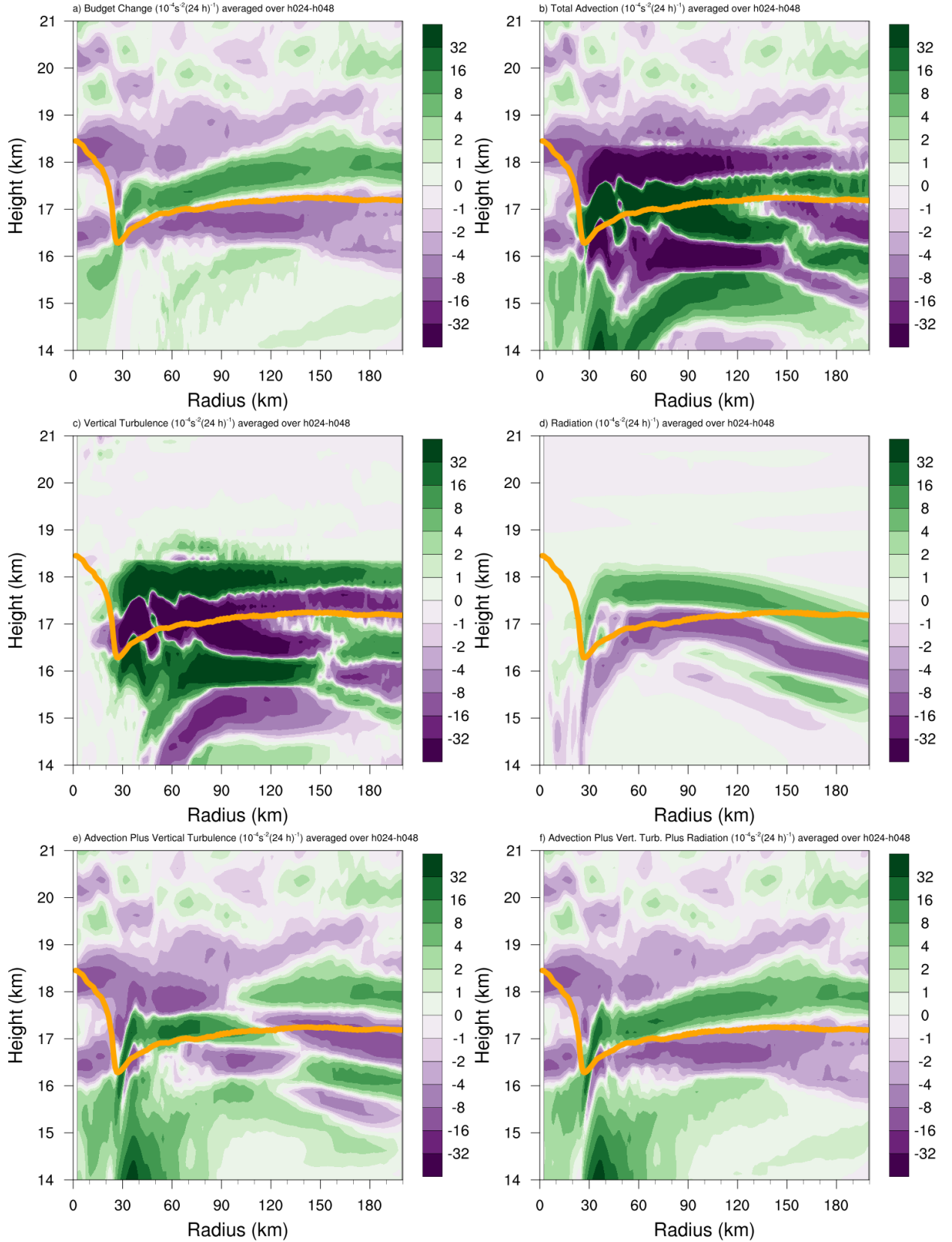


FIG. 6. As in Fig. 5, but for the 24-48-hour period.



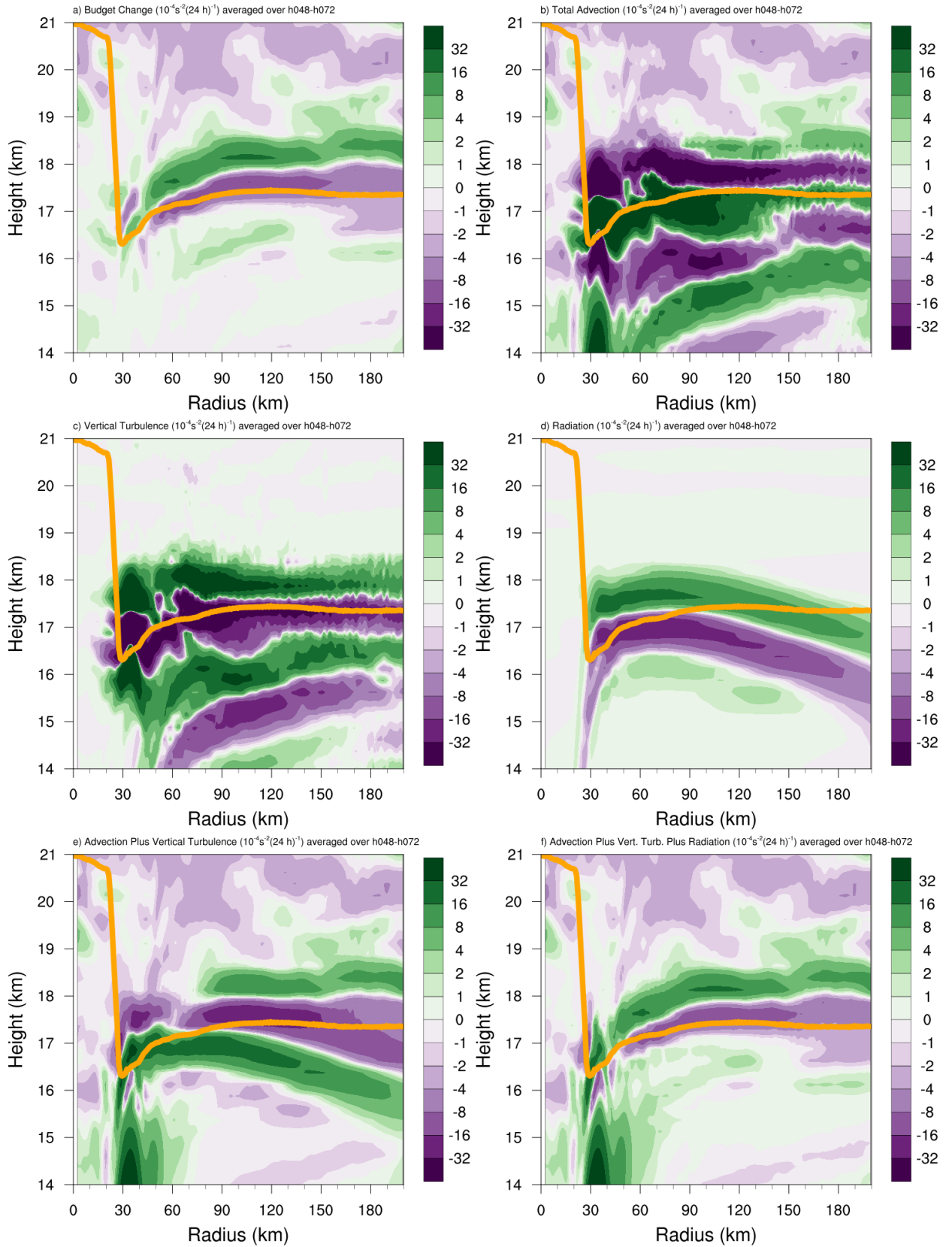


FIG. 7. As in Fig. 5, but for the 48-72-hour period.

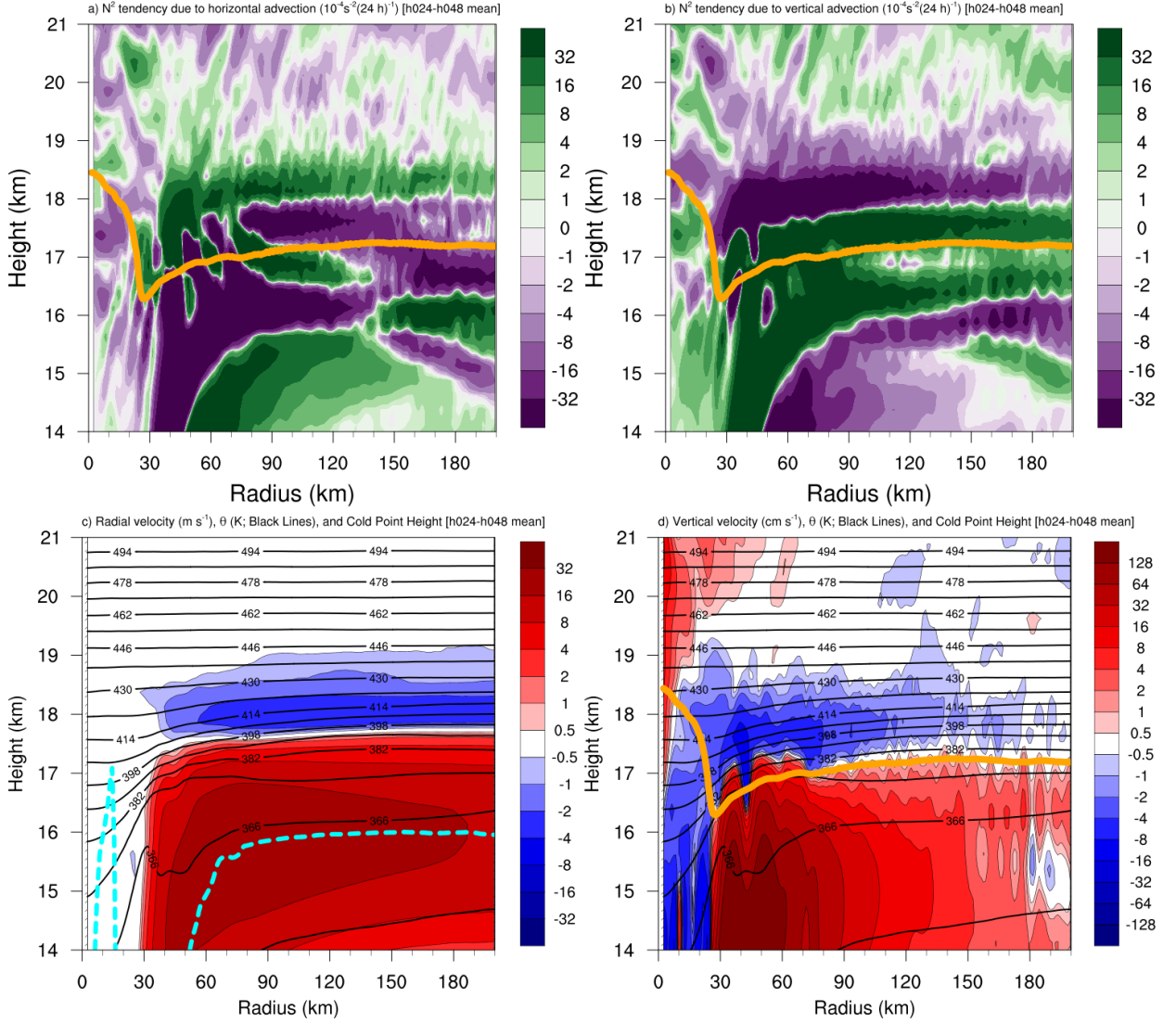
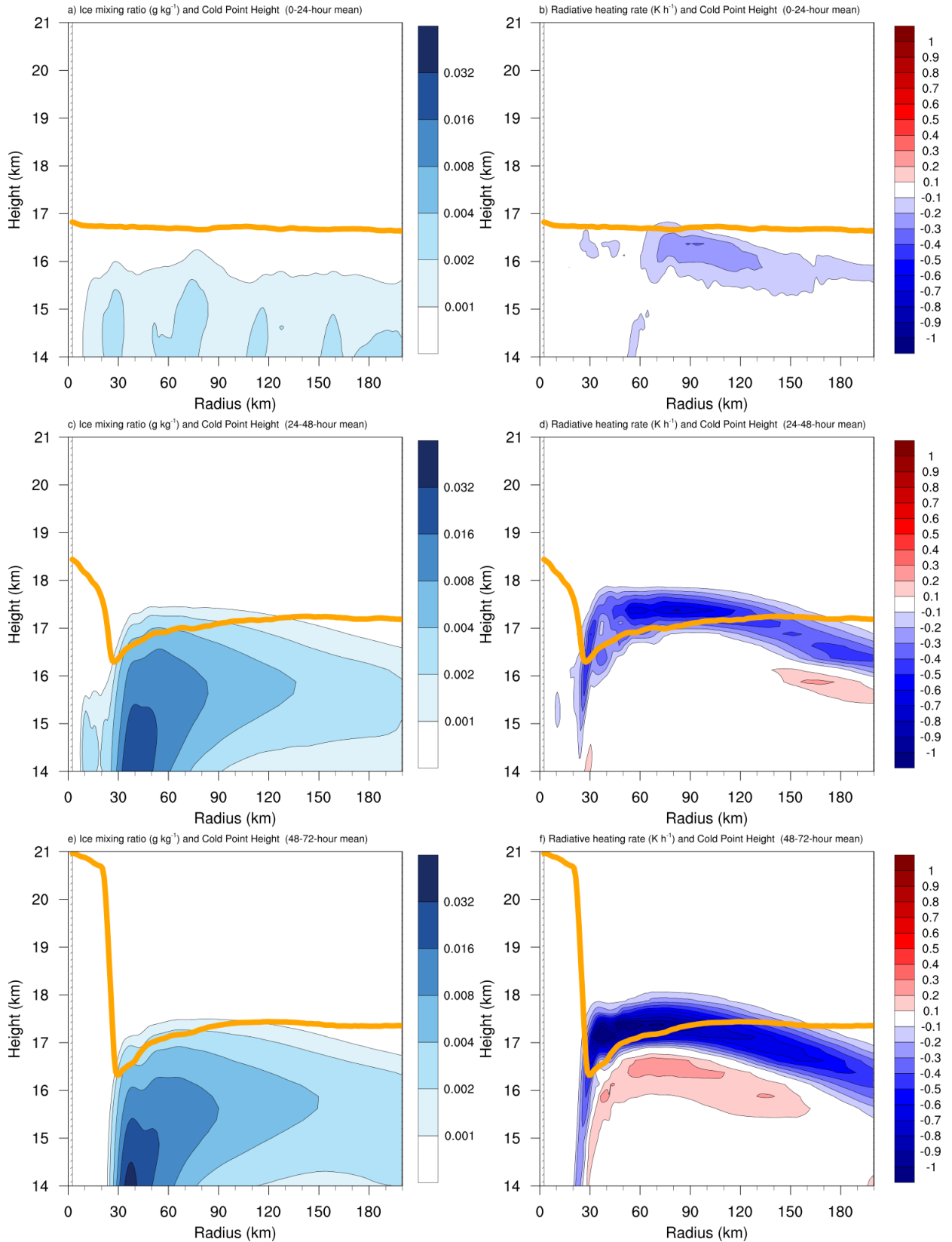


FIG. 8. The contributions to the change in  $N^2$  over the 24-48-hour period ( $10^{-4} \text{ s}^{-2} (24 \text{ h})^{-1}$ ) by (a) horizontal advection and (b) vertical advection. (c) The radial velocity ( $\text{m s}^{-1}$ ; filled contours), potential temperature (K; thick black contours), cold-point tropopause height (orange line), and level of maximum outflow (dashed cyan line) averaged over the 24-48-hour period. (d) The vertical velocity ( $\text{cm s}^{-1}$ ; filled contours), potential temperature (K; thick black contours), and cold-point tropopause height (orange line) averaged over the 24-48-hour period.



525 FIG. 9. Ice mixing ratio ( $\text{g kg}^{-1}$ ) and cold-point tropopause height (orange lines) averaged over (a) 0-24 hours,  
526 (c) 24-48 hours, and (e) 48-72 hours. Radiative heating rate ( $\text{K h}^{-1}$ ) and cold-point tropopause height (orange  
527 lines) averaged over (b) 0-24 hours, (d) 24-48 hours, and (f) 48-72 hours.

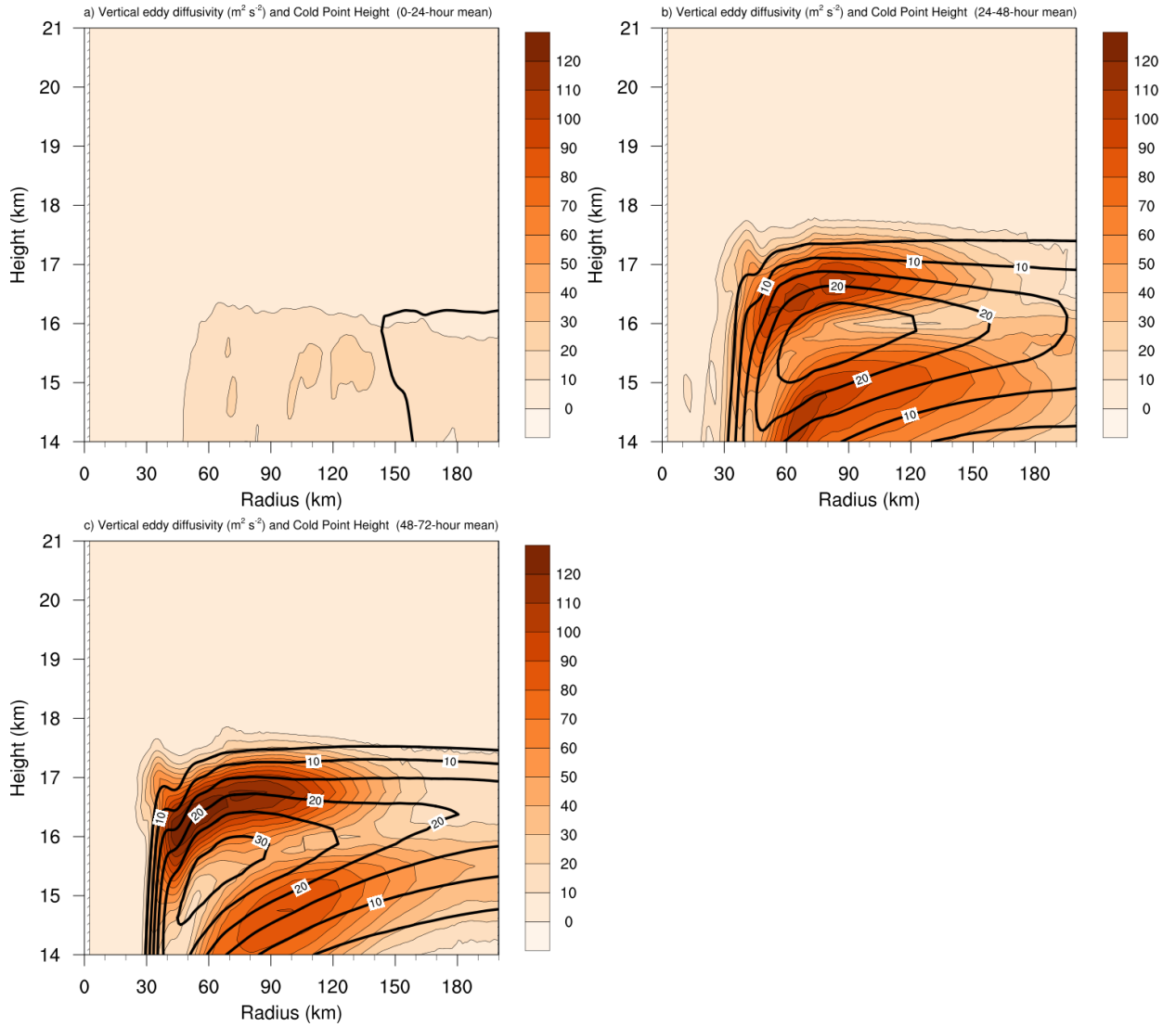
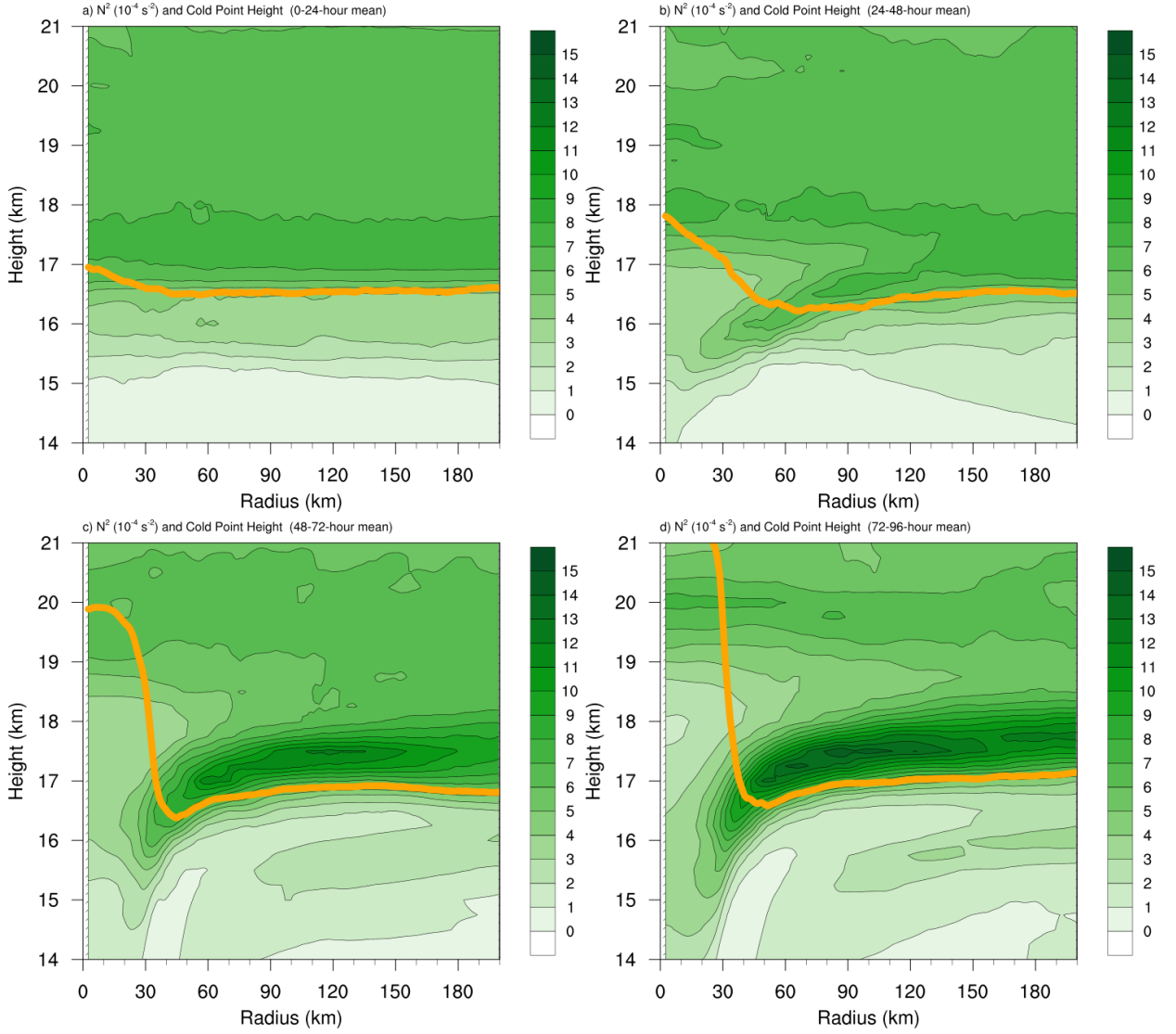


FIG. 10. Vertical eddy diffusivity ( $\text{m}^2 \text{s}^{-2}$ ; filled contours), cold-point tropopause height (cyan lines), and radial velocity ( $\text{m s}^{-1}$ ; thick black lines) averaged over (a) 0-24 hours, (b) 24-48 hours, and (c) 48-72 hours.



530 Fig. A1. Twenty-four-hour averages of squared Brunt-Väisälä frequency ( $N^2$ ;  $10^{-4} \text{ s}^{-2}$ ) over (a) 0-24 hours,  
 531 (b) 24-48 hours, (c) 48-72 hours, and (d) 72-96 hours for the simulation described in Appendix Aa. Orange lines  
 532 represent the cold-point tropopause height averaged over the same time periods.

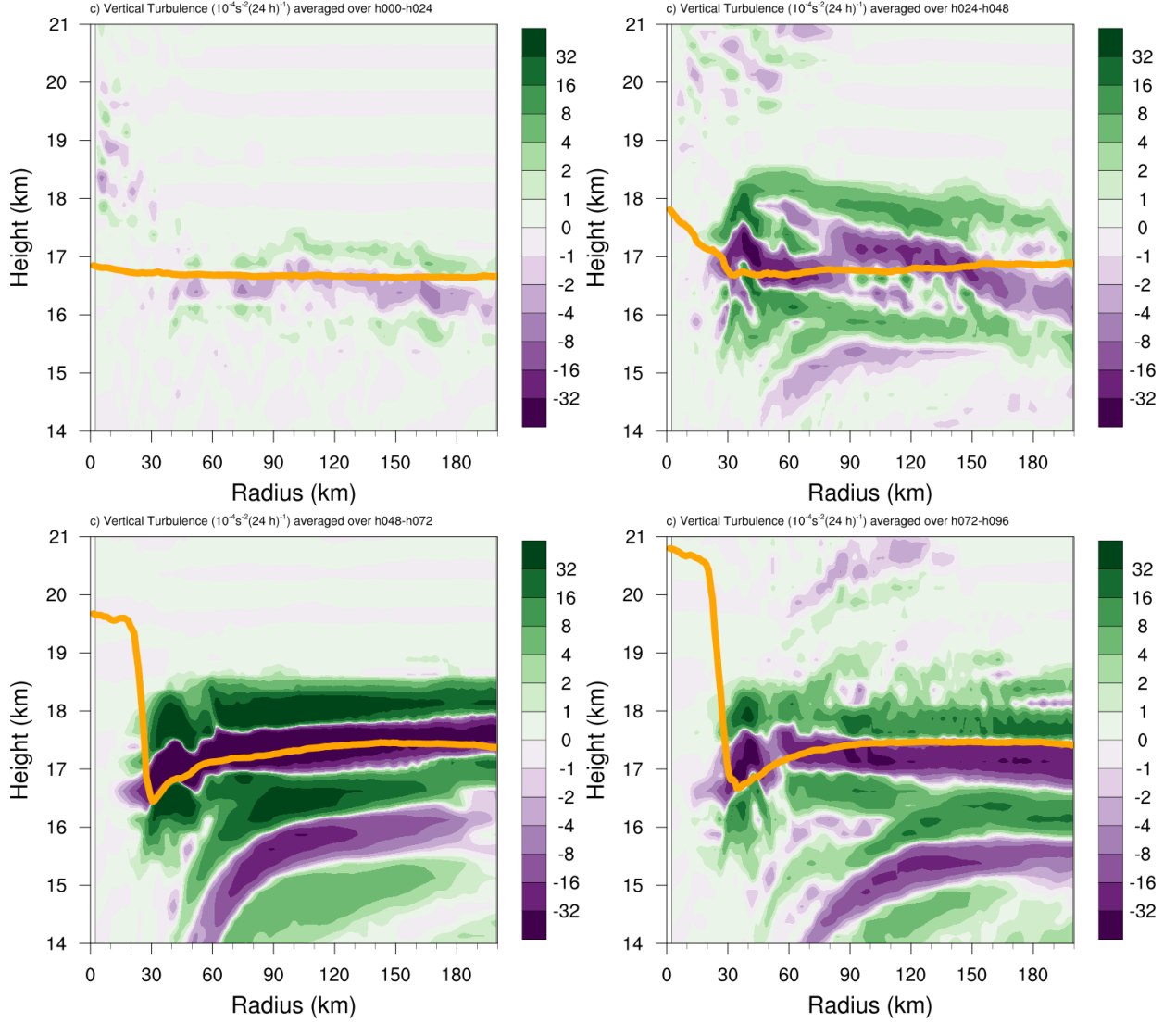


Fig. A2. The contribution of vertical turbulence to the  $N^2$  variability ( $10^{-4} \text{ s}^{-2} (24 \text{ h})^{-1}$ ) averaged over (a) 0-24 hours, (b) 24-48 hours, (c) 48-72 hours, and (d) 72-96 hours for the simulation described in Appendix Ab. Orange lines represent the cold-point tropopause height averaged over the same time periods.